Carbon quantum dots as nano-scaffolds for α-Fe_2O_3 growth: Preparation of Ti/CQD@α-Fe_2O_3 photoanode for water splitting under visible light irradiation

Omran Moradlou*[,a], Zeinab Rabiei[a], Alireza Banazadeh[b], Juliusz Warzywoda[c], Mohammad Zirak[d]

[a]*Department of Chemistry, Alzahra University, P.O. Box: 1993893973, Tehran, Iran*

[b]*Department of Chemistry and Biochemistry, Texas Tech University, Lubbock, TX, USA*

[c]*Materials Characterization Center, Whitacre College of Engineering, Texas Tech University, Lubbock, TX 79409-3103, USA*

[d]*Department of Physics, Hakim Sabzevari University, P.O. Box 961797648, Sabzevar, Iran*

E-mail: moradlou@alzahra.ac.ir

Abstract

To improve the photoresponsivity of hematite-based photoanode via better charge transfer rate and short paths for the electron transport, carbon quantum dots (CQDs) were used as conductive nano-scaffolds for the growth of photoactive material on Ti substrate. CQDs@α-Fe_2O_3 nanoparticulates with the average diameter of 3-5 nm were uniformly grown on the substrate under the finely optimized experimental conditions to prepare Ti/CQDs@α-Fe_2O_3 photoanode. The photocurrent response of the resulted photoanode with a photocurrent density of 2.1 $mAcm^{-2}$ at applied E_{bias} of +0.5V *vs.* Ag/AgCl was increased by a factor of 10 compared to Ti/α-Fe_2O_3, mainly due to the improvement in charge-transfer rate and suppression of electron-hole recombination derived from the increased hole-diffusion length in conducting nano-scaffold structure. The surface morphology of samples was investigated with FE-SEM and HRTEM. Charge transfer resistance (R_{ct}) of Ti/α-Fe_2O_3 and Ti/CQDs@α-Fe_2O_3 photoanodes were estimated to be about 90.9 and 3.7 KΩ, respectively. After the continuous 4 h illumination of Ti/CQDs@α-Fe_2O_3 photoanode under the visible light irradiation, the efficiency of water splitting process (i.e. the photocurrent) did not changed significantly (±5%), indicating the high stability of photoanode and tightly deposited CQDs@α-Fe_2O_3 on Ti substrate, which was confirmed by FE-SEM image of the sample after the experiment. The formation of carbon-oxygen chemical bonds between CQDs and hematite molecules was confirmed by X-ray

photoelectron spectroscopy (XPS). Finally, based on XRD pattern and photoresponses of various photoanodes annealed at different temperatures, the results showed that the structure design is as significant as crystallinity in hematite-based photoelectrodes.

Keywords: Hematite; CQD; nanostructuring; water splitting

1. Introduction

Hematite, α-Fe_2O_3, has been identified as an excellent semiconductor material for the fabrication of photoanodes in photoelectrochemical (PEC) water splitting processes because of its good chemical and photoelectrochemical stability, earth-abundance, low cost, environmental friendliness and having a narrow energy band gap (E_g) of about 2.2 eV with the valence band edge position below the water oxidation potential [1, 2]. The main drawbacks of hematite as a photoactive semiconductor are the short hole-diffusion length (a few nanometers without bias and tens of nanometers with bias), poor hole mobility (0.01 cm^2V^{-1} s^{-1}) and hole lifetime, high overvoltage (i.e. slow kinetics) of the oxygen evolution reaction and the electron-hole recombination [3]. Among these problems, the short hole-diffusion length within hematite is an important limiting factor [4].

Several strategies have been developed to address these limitations including: (a) doping the elements (Ti, Nb, Mo, Si, etc.) to introduce additional mobile charge carriers [2,5]; (b) introducing intermediate layer at hematite/substrate interface to enhance the hole transport; (c) introducing water oxidation catalyst such as cobalt-phosphate (Co-Pi) [6-8] and IrO_2 [9] on hematite film to accelerate water oxidation kinetics; (d) passivating the surface trapping states of hematite with overlayer deposition with Al_2O_3 [10], Fe_2TiO_5 [3], SnO_x [11] or heterojunctions to reduce the surface electron-hole recombination; and finally, (e) control of crystallinity [12] and (f) morphology [13] of hematite.

It is believed that the deposition of highly crystalline hematite on the substrate is the best way to enhance the charge separation [12-15]. However, even in single crystal hematite films, the short hole-diffusion length within hematite remains unsolved.

In this respect, to achieve a balance between light harvesting and hole collection, the overall photoactive material morphology should be kept in nanoscale. Vertically aligned nanorods [16]

and worm-like structure [12,17] are two ideal morphologies for PEC applications of α-Fe_2O_3. Nanorods can overcome hole transport limitations, because the photoexcited electrons could flow through a direct pathway along the axial direction of rods [18]. As a drawback for the nanoscale morphology, nanostructuring offers longer paths for the electron transport to the conductive substrate and increases the probability of electron-hole recombination [13].

So, an appropriate approach would be the synthesis of crystalline hematite with the nanostructured morphology having a reasonable conductivity, better charge transfer rate and short paths for the electron transport. Base on this idea, this work aims the use of carbon quantum dots (CQDs) as nano-scaffolds for the growth of α-Fe_2O_3 on conductive substrate under the finely optimized experimental conditions.

Experimental

Fabrication of Ti/α-Fe_2O_3 and Ti/CQD@α-Fe_2O_3 photoanode

The electrochemical method was used for the synthesis of CQDs as reported elsewhere [20] by using two graphite rods (as anode and cathode) immersed in a 100 ml solution of ethanol:H_2O (99:1) containing 0.30 g NaOH under the applied constant current intensity of 180 mA cm^{-2} for 24h.

For the fabrication of Ti/CQD@α-Fe_2O_3 photoanode, hydrothermal method was used. Typically, in an aqueous solution of 0.1 mg mL^{-1} CQD (10.0 mL), an appropriate amounts of Fe^{3+} (0.05 M) and $NaNO_3$ (1.0 M) were added and the pH of solution was adjusted to 1.40 (by adding concentrated HCl) and stirred for 15 min. The mixture was then transferred to a highly cleaned 50-mL Teflon-lined stainless steel autoclave, and a pre-cleaned Ti sheet (3×1 cm^2) was immersed vertically into the solution and heated to 100˚C for 6 h. Ti substrate which was coated with yellow-orange thin film of CQD@α-Fe_2O_3 was annealed at 390 ℃ for 2 h. For the fabrication of Ti/α-Fe_2O_3 using hydrothermal method, the same procedure was used where the CQD solution was replaced with DI water.

PEC measurements

The photoresponse was investigated in a three-electrode electrochemical cell with a Ti/CQD@α-Fe_2O_3 photoanode as working electrode, a platinum plate as a counter electrode and an Ag/AgCl (KCl 3.0 M) as a reference electrode. The electrochemical measurements were carried out using

a Galvanostat/Potentiostat Autolab PGSTAT101 instrument. The electrochemical impedance spectroscopy (EIS) of the samples was studied by Autolab PGSTAT 302N equipped with FRA Impedance Module. During all PEC measurements, 0.5 M KOH was used as electrolyte.

3. Results and Discussion

The characterization of Ti/α-Fe_2O_3 and Ti/CQD@α-Fe_2O_3 photoanodes including their surface morphology, crystal phase and energy band gaps (E_g) was investigated. Ti/α-Fe_2O_3 photoanodes were fabricated by using two methods, i.e. hydrothermal method and successive ion layer adsorption and reaction (SILAR) process. In hydrothermal reaction method, the effects of main experimental conditions including Fe^{3+} precursor concentration and reaction time were studied. In this respect, six Ti/α-Fe_2O_3 samples were prepared according to the conditions included in Table 1.

(**Table 1**)

Morphology of Ti/α-Fe_2O_3 and Ti/CQD@α-Fe_2O_3 photoanodes

Six Ti/α-Fe_2O_3 samples were prepared by using hydrothermal method at different Fe^{3+} precursor concentrations and the hydrothermal reaction times (**Table 1**). **Fig. 1a** shows the FE-SEM image of Ti/α-Fe_2O_3-L6h sample prepared under the experimental conditions including Fe^{3+} precursor concentration of 0.05 M and the hydrothermal reaction time of 6 h. As it is clear, the morphology of hydrothermally prepared α-Fe_2O_3 is 1-D nanorod. HRTEM images of α-Fe_2O_3 samples were also investigated. **Fig. 1b** shows the TEM image of Ti/α-Fe_2O_3-L6h sample. The average diameter of α-Fe_2O_3 nanorods is about 25 nm and their average length is about 200 nm, confirming the FE-SEM results. The SEM-EDS map of the sample (Fig. 1c) shows the uniform distribution of Fe element on Ti substrate.

It seems that the hydrothermal synthesis of α-Fe_2O_3 nanorods follows two stages including the initial nucleation of rod-like akaganeite nuclei [22] and the subsequent ripening of nuclei together to form akaganeite (β-FeOOH) nanorods would then transform to hematite (α-Fe_2O_3) nanorods by annealing. On the other hand, in the synthesis of Ti/α-Fe_2O_3-n samples by SILAR method, the morphology of the as-deposited iron oxide thin film is nanoparticle with the average grain size of about 30 nm.

(**Fig. 1**)

The electrochemically synthesized CQDs were characterized with HRTEM and photoluminescence (PL) spectroscopy. **Figure 2a** shows high-resolution TEM image of CQDs with the average diameter of 2.0 nm with the lattice spacing of around 0.31 nm, which agrees well with <002> spacing of graphitic carbon [20,23,24]. To investigate the optical properties of as-synthesized CQDs, the study was carried out by using different excitation wavelengths (λ_{ex}) of 240, 300, 360 and 420 nm (**Fig. 2b**). As it is clear, CQDs give visible light emission in the range of 300-600 nm. B varying the λ_{ex}, the wavelength of PL with maximum intensity (λ_{em}) shifts to the longer wavelengths (Red shift), which is the characteristics optical properties of CQDs.

(**Fig. 2**)

The surface morphology of the fabricated Ti/CQD@α-Fe_2O_3 photoanode was characterized with FE-SEM (**Fig. 3a**) and SEM mapping (**Fig. 3b and c**). To confirm the FE-SEM results, morphology of CQD@α-Fe_2O_3 was examined with HRTEM (**Fig. 3d** and **e**). The HRTEM images clearly show that CQDs with the average size of 2 nm act as nano-scaffolds to form uniform CQDs@α-Fe_2O_3 nanoparticulates on the substrate. So, it can be concluded that CQDs can serve as the nucleation sites for the growth of $Fe(OH)_3$ nuclei around CQDs resulting CQD@α-Fe_2O_3 nanoparticulates with the average size of 3-5 nm. From the selected area electron diffraction (SAED) pattern of α-Fe_2O_3 at CQD@α-Fe_2O_3 nanoparticulates (**Fig. 3g**), the spacing values of the lattice fringes were determined to be 3.624, 2.657 and 2.173 Å, which can be indexed to hematite α-Fe_2O_3 [25,26].

(**Fig. 3**)

Crystal phase and spectroscopic characterizations of photoanodes

The typical XRD patterns of α-Fe_2O_3 and CQD@α-Fe_2O_3 nanocomposites are shown in **Fig. 4a**. The characteristic diffraction peaks for α-Fe_2O_3 and CQD@α-Fe_2O_3 samples were observed at 2θ values of 24.1019˚, 33.0966˚, 35.6004˚, 40.8064˚, 49.4007˚, 53.9896˚, 57.4886˚, 62.3551˚ and

63.9145˚, attributed to (012), (104), (110), (113), (024), (116), (122), (214) and (300) crystal planes, respectively.

(**Fig. 4**)

Band gap energy (E_g) of the hydrothermally fabricated photoanodes were calculated from diffuse reflectance spectral (DRS) data (**Fig. 4b**) and plot of $(\alpha h\upsilon)^2$ *vs.* photon energy ($h\upsilon$) (**Fig. 4c**) E_g's of Ti/α-Fe_2O_3 and Ti/CQD@α-Fe_2O_3 samples were obtained to be 2.10 eV and 2.05 eV, respectively. The surface chemical composition of the synthesized samples was characterized by X-ray photoelectron spectroscopy (XPS). Full XPS spectrum (survey spectrum) of CQD@α-Fe_2O_3 surface has been shown in **Fig. 5**. High resolution XPS scans (XPS windows) of Fe 2p core level (Fig. 5b) shows two distinct peaks with binding energies (BE) of 723.3 and 710.1 eV, which are assigned to Fe $2p_{1/2}$ and Fe $2p_{3/2}$ energy levels, respectively [27-30]. The observed BE difference between these two peaks is 13.2 eV arising from the spin-orbit splitting effect. A weak satellite Fe^{3+} peak is also observed at 718 eV. These peaks are ascribed to 3+ oxidation state of Fe, verifying the formation of α-Fe_2O_3 stoichiometry [28,29]. Fig. 5c shows XPS window of C 1s core level. This spectrum exhibits two main peaks centered at 285 (named as A) and 290 eV (named as B), which are attributed to carbon-carbon and carbon-oxygen bonds, respectively [27-29,31-33]. The A peak has been deconvoluted to two peaks with BE of 285.0 and 286.3 eV which are attributed to C-C and C=C bonds of CQDs, respectively [27,29,32]. The peak B has been curve fitted by two peaks located at BE values of 289.4 and 290.6 eV which are assigned to C-O and C=O bonds, respectively [27,29,32]. The presence of B peak (carbon-oxygen bonds) with remarkable intensity as compared to A peak (carbon-carbon bonds), revealed that the chemical bonds exist between C atoms of CQDs and O atoms of hematite, similar two XPS spectrum of C 1s for iron carbonate [33]. O 1s XPS window curve fitting confirm the formation of carbon-oxygen chemical bonds.

(Fig. 5)

Electrochemical performance of photoanodes

Linear sweep voltammetry (LSV) was used to investigate the onset potential of water oxidation and photoactivity of samples. The photocurrent densities (J_{ph}/mAcm^{-2}) of Ti/α-Fe_2O_3 and

Ti/CQD@α-Fe_2O_3 photoelectrodes were measured in both dark and illuminating conditions as a function of applied bias from 0 to 1.0 V (**Fig. 6a**). A distinguished 150 mV cathodic shift of onset potential at Ti/CQD@α-Fe_2O_3 electrode surface indicates the lower overpotential toward water oxidation. Under the visible light irradiation, the electron-hole pairs are generated at the surface of both photoanodes when the applied bias is reached to the onset potential of about 0.2 V (Fig. 6a). The obtained onset potential under the visible light irradiation is lower than or comparable with the previously reported α-Fe_2O_3-based photoanodes (**Table 2**).

(**Table 2**)

Under the illumination conditions, the measured J_{ph} for Ti/CQD@α-Fe_2O_3 photoanode as a function of applied potential (J_{ph} vs. E_{bias}) at different illumination intensities (I_{light}) were also depicted in **Fig. 6b**. The photocurrent density (J_{ph}) of the Ti/CQD@α-Fe_2O_3 photoanode was increased with the increase of incident light intensity. A diagram of J_{ph} versus I_{Light} was drawn at 0.5 V potential (**Fig. 6c**).

(**Fig. 6**)

Electrochemical impedance spectroscopy

It is implied from the LSV of Ti/CQD@α-Fe_2O_3 photoanode that CQDs may improve the charge transfer in nanostructured CQD@α-Fe_2O_3. The Nyquist plots and the equivalent circuit model have been shown in **Fig. 7**. From the Nyquist plots and the equivalent circuits resulted from the data fitting, R_{ct} corresponding to Ti/α-Fe_2O_3 and Ti/CQD@α-Fe_2O_3 samples were obtained to be 90.9 KΩ and 3.7 KΩ, respectively. The main difference between Nyquist plots of these two samples is the semi-circle at higher frequencies that this part of EIS plot mainly corresponds to the e^--h^+ recombination in bulk of photoactive material. This can be explained by the morphology differences in these two samples and their conductivities. In fact, the photo-generated e^--h^+ pairs at the surface of CQD@α-Fe_2O_3 nanoparticles (with the size of about 5.0 nm and lower R_{ct}) have more tendency to flow through the surface of particles compared to α-Fe_2O_3 nanorods (with the diameter of about 25 nm and higher R_{ct}). So, it seems that the nanostructuring of α-Fe_2O_3 with CQDs results the faster hole transfer in bulk of material

nanostructure. Consequently, significantly reduced R_{ct} and the accelerated electron transfer rate indicate a strong influence of CQDs embedded in CQD@α-Fe_2O_3 nanostructure on the interfacial kinetics.

(**Fig. 7**)

Photoresponsivity of Ti/α-Fe_2O_3 and Ti/CQD@α-Fe_2O_3

To study the photoresponsivity of the fabricated samples, chronoamperometric technique was used at an applied E_{bias} of +0.5 V under dark and illumination conditions. Chronoamperograms of Ti/α-Fe_2O_3 and Ti/CQD@α-Fe_2O_3 photoanodes prepared by using hydrothermal method (4 samples) are shown in **Fig. 8a**. As it is clear from the results, very rapid generation of photocurrent densities (J_{ph}) was observed for all photoanodes upon visible illumination. The anodic current spike is not occurred for these samples when the light is on, indicating the lack of photogenerated hole accumulation at the electrode surface because of the fast water oxidation reaction. The cathodic current spike was not observed when the light was off, due to the lower e^--h^+ recombination.

Because of the important role of CQDs in photoresponse of hematite-based photoanodes, the effect of concentration and size of CQDs on the photocurrent density of Ti/CQDs@α-Fe_2O_3 was investigated. Beyond the optimized CQDs concentration, photocurrent density was not change drastically. So, the optimum photoanode is Ti/CQD@α-Fe_2O_3 with highest J_{ph} of 2.1 mA cm^{-2}. The stability of the sample was examined by the illumination of photoanode under the visible light irradiation and the applied bias of +0.5 V for 4 h in a tightly sealed and de-aerated 3-electrode electrochemical cell. The resulted I-t curve and the time course of O_2 evolution are shown in **Fig. 8c and d**, respectively. After the continuous 4 h irradiation, J_{ph} did not changed significantly (±5%), indicating the high stability of photoanode and tightly deposited CQDs@α-Fe_2O_3 on Ti substrate, which was confirmed by FE-SEM image of the sample after the experiment (Fig. S2).

(**Fig. 8**)

(**Fig. 9**)

(**Table 3**)

It should be noted that J_{ph} of optimized Ti/α-Fe_2O_3-100 sample fabricated by SILAR method (with J_{ph} of 1.50 $mAcm^{-2}$) is about 2 times higher than that of optimized Ti/α-Fe_2O_3-L6h sample prepared by hydrothermal method (with J_{ph} of 0.8 $mAcm^{-2}$). This can be explained by the effect of thickness of α-Fe_2O_3 deposited on substrate. The average thicknesses of Ti/α-Fe_2O_3-L6h and Ti/α-Fe_2O_3-100 samples are ~100 nm and ~50 nm, respectively, obtained from cross-section FE-SEM images (**Figures S1 and S3**). So, from these findings, it seems that the film thickness is a crucial factor that should be controlled in the fabrication of α-Fe_2O_3-based photoanodes

Chronopotentiometry

The photo-potential of Ti/CQD@α-Fe_2O_3 is lower than that of Ti/α-Fe_2O_3 photoanode, indicating that the free electron density is increased in CQD@α-Fe_2O_3 under similar illumination condition [47]. So, there are more photoelectrons accumulated on the surface of Ti/CQD@α-Fe_2O_3 compared to Ti/α-Fe_2O_3. As **Fig. 10a** shows, under the illumination, the Fermi level of two samples is negatively shifted and when the light is off, the photo-generated charges leak out of the substrate. Open-circuit voltage (V_{oc}) values for Ti/CQD@α-Fe_2O_3 and Ti/α-Fe_2O_3 samples are -0.31 V and -0.2 1V, respectively. The electron life time (τ_n) for Ti/CQD@α-Fe_2O_3 and Ti/α-Fe_2O_3 samples were calculated to be 240 and 110 ms, respectively. So, the photo-generated carrier life time is increased in CQD@α-Fe_2O_3.

(**Fig. 10**)

The band structure of photoactive CQD@α-Fe_2O_3 is schematically represented in **Fig. 10b**. As confirmed by HRTEM images (**Fig. 3e**), at CQD@α-Fe_2O_3 nanoparticulates, CQDs act as core for the growth of α-Fe_2O_3 shell. So, by the irradiation of CQD@α-Fe_2O_3, α-Fe_2O_3 shell will act as light absorber material. The results of chronopotentiometric technique showed that the photopotential of Ti/CQD@α-Fe_2O_3 is lower than that of Ti/α-Fe_2O_3 photoanode, indicating that the free electron density is increased in CQD@α-Fe_2O_3 under similar illumination condition. Under the illumination, the Fermi level of Ti/CQD@α-Fe_2O_3 sample is more negatively shifted compare to Ti/α-Fe_2O_3. More negative open circuit potential (V_{oc}) and higher electron life time (τ_n) for Ti/CQD@α-Fe_2O_3 indicate that the minority carrier (h^+) accumulation and e^--h^+ recombination is reduced at the surface of Ti/CQD@α-Fe_2O_3 sample. The probable mechanism

for describing the enhanced photoactivity CQD@α-Fe_2O_3 compared to α-Fe_2O_3 is the h^+ transfer (or h^+ hopping) from valence band (VB) of α-Fe_2O_3 to the HOMO of CQDs (**Fig. 10b**).

Careful curve fitting of high resolution XPS data revealed that C-O bonds are attributed to chemical bond between carbon and oxygen atoms of CQDs and α-Fe_2O_3. Thus, the hole transfer between CQDs and α-Fe_2O_3 is more feasible. Because of the short hole-diffusion length in the structure of α-Fe_2O_3, nanostructuring by CQD (which was confirmed by HRTEM in this work) causes the faster hole transportation by CQDs in CQD@α-Fe_2O_3 and reduces the e^--h^+ recombination. So, h^+ hopping from the VB of α-Fe_2O_3 to HOMO CQDs can be expected.

4. Conclusions

An appropriate approach for the fabrication of hematite-based photoanode with high photocurrent density is the structure design with nanostructured morphology. So, in this respect, Ti/CQD@α-Fe_2O_3 photoanode was proposed because of the suppressed electron-hole recombination, higher charge transfer rate and faster water oxidation kinetics at the surface of photoelectrode.

Acknowledgements

The authors would like to thank Research Council of Alzahra University for financial support.

Figure Captions

Fig. 1. (a) FE-SEM image of α-Fe_2O_3 nanorods grown on Ti substrate by hydrothermal method (Ti/α-Fe_2O_3-L6h sample). (b) HRTEM image of α-Fe_2O_3 nanorods of Ti/α-Fe_2O_3-L6h. (c) FE-SEM mapping image of Fe in Ti/α-Fe_2O_3-L6h sample. The experimental conditions for the fabrication of Ti/α-Fe_2O_3-L6h sample were: Fe^{3+} precursor concentration of 0.05 M, $NaNO_3$ concentration of 1.0 M, hydrothermal reaction temperature of 100˚C and reaction time of 6 h. (d) FE-SEM image of Ti/α-Fe_2O_3-100 prepared by SILAR method.

Fig. 2. (a) HRTEM image of CQDs. (b) PL spectra of electrochemically synthesized CQDs at various excitation wavelengths of 240, 300, 360 and 420 nm.

Fig. 3. (a) FE-SEM image (top view) from Ti/CQD@α-Fe_2O_3 photoanode fabricated by hydrothermal method. (b and c) FE-SEM mapping image of Fe (b) and carbon (c) in

Ti/CQD@α-Fe_2O_3 sample. (d and e) HRTEM image of CQD@α-Fe_2O_3 naoparticulates at different magnifications. (f) HRTEM image of CQD@α-Fe_2O_3 synthesized at Fe^{3+} precursor concentration of 0.15 M, $NaNO_3$ concentration of 1.0 M, hydrothermal reaction temperature of 100˚C and reaction time of 6 h. (g) Selected area electron diffraction (SAED) pattern of α-Fe_2O_3 in CQD@α-Fe_2O_3.

Fig. 4. (a) XRD patterns of α-Fe_2O_3 and CQD@α-Fe_2O_3. (b) Diffuse reflectance spectra (DRS) of Ti/α-Fe_2O_3 and Ti/CQD@α-Fe_2O_3 photoanodes. (c) Plot of $(\alpha h\upsilon)^2$ *vs.* photon energy ($h\upsilon$, eV) of photoanodes.

Fig. 5. (a) XPS survey spectrum of CQD@α-Fe_2O_3. High resolution XPS scans of Fe 2p (b), C 1s (c) and O 1s (d) core levels.

Fig. 6. (a) LSV of Ti/α-Fe_2O_3 and Ti/CQD@α-Fe_2O_3 photoanodes at the scan rate of 0.1 Vs^{-1}, (b) LSV of Ti/CQD@α-Fe_2O_3 photoanode at different illumination intensities under the illumination conditions. (c) Diagram of J_{ph} versus I_{Light} at +0.5 V bias potential.

Fig. 7. (a) Nyquist plots of Ti/α-Fe_2O_3 and Ti/CQD@α-Fe_2O_3 electrodes, (b) the equivalent circuits resulted from the data fitting by Zview.

Fig. 8. (a) Photocurrent density response of Ti/α-Fe_2O_3 photoanodes annealed at 390˚C, 500˚C and 600˚C and Ti/CQD@α-Fe_2O_3 photoanode annealed at 390˚C. (b) Photoresponse of Ti/CQD@α-Fe_2O_3 samples prepared with different CQDs synthesized under the applied constant current densities of 20, 100 and 180 mA cm^{-2}. (c) Photoresponse of Ti/CQD@α-Fe_2O_3 under the visible light irradiation during 4 h illumination. (d) Time course of O_2 evolution from KOH 0.5 M solution with Ti/CQD@α-Fe_2O_3 photoanode under visible light irradiation. All of the experiments were performed in 0.5 M KOH at an applied bias of +0.5 V *vs.* Ag/AgCl.

Fig. 9. (a) Photoresponse of Ti/α-Fe_2O_3-n photoanodes fabricated by SILAR method at different SILAR cycles of 10, 20, 30, 50, 100 and 150 cycles and annealed at 500˚C. (b) Photocurrent density of Ti/α-Fe_2O_3-n as a function of SILAR cycles (n).

Fig. 10. (a) Open circuit photo-voltage in light on-off process for Ti/α-Fe_2O_3 and Ti/CQD@α-Fe_2O_3 samples. (b) Schematic diagram for band structure of CQD@α-Fe_2O_3 and the possible mechanism of e^--h^+ transfer in illuminated photoanode. (c) %IPCE of the samples versus irradiated wavelength (nm) under constant illumination intensity (100 mW cm^{-2}).

Fig. 1

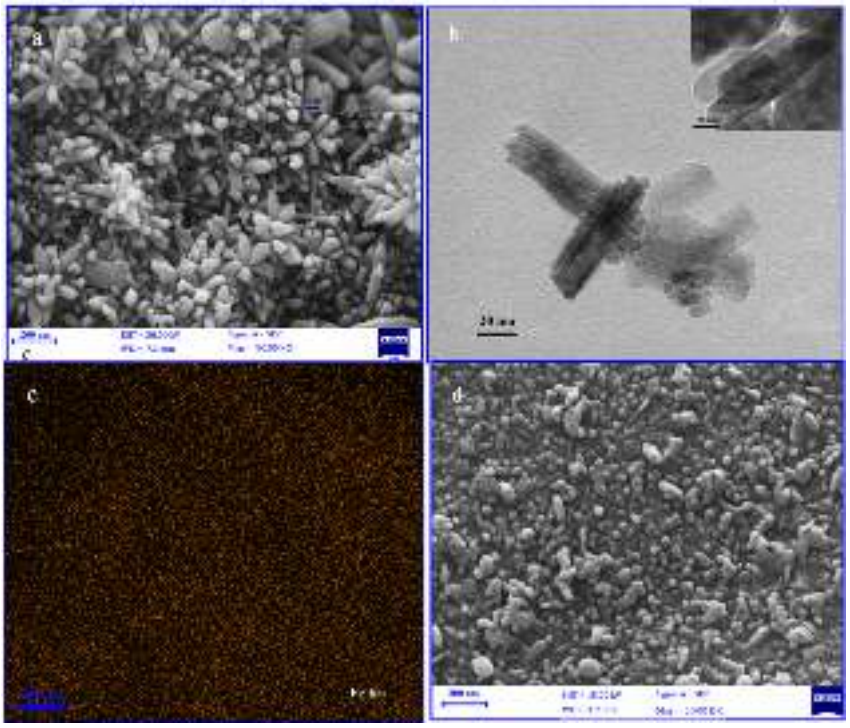

Fig. 2

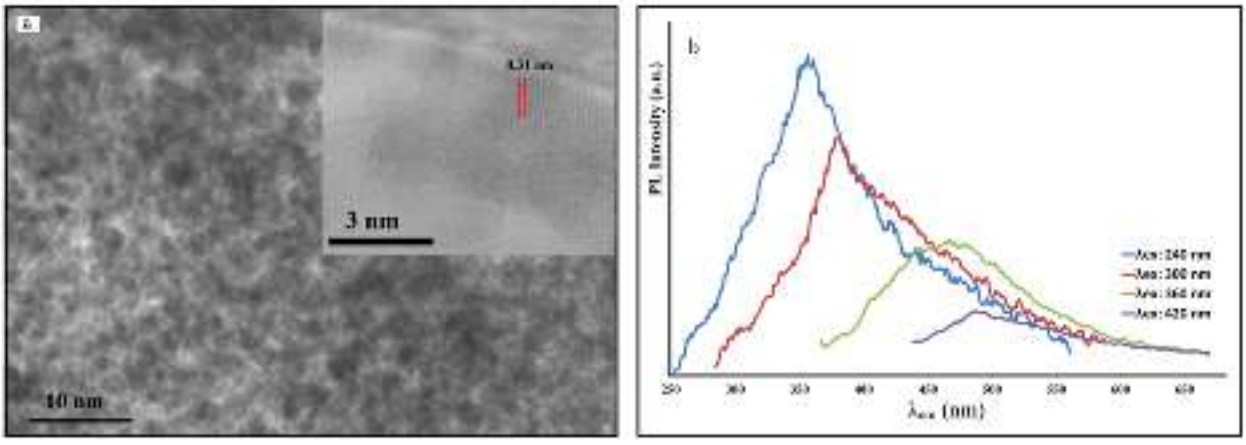

Fig. 3

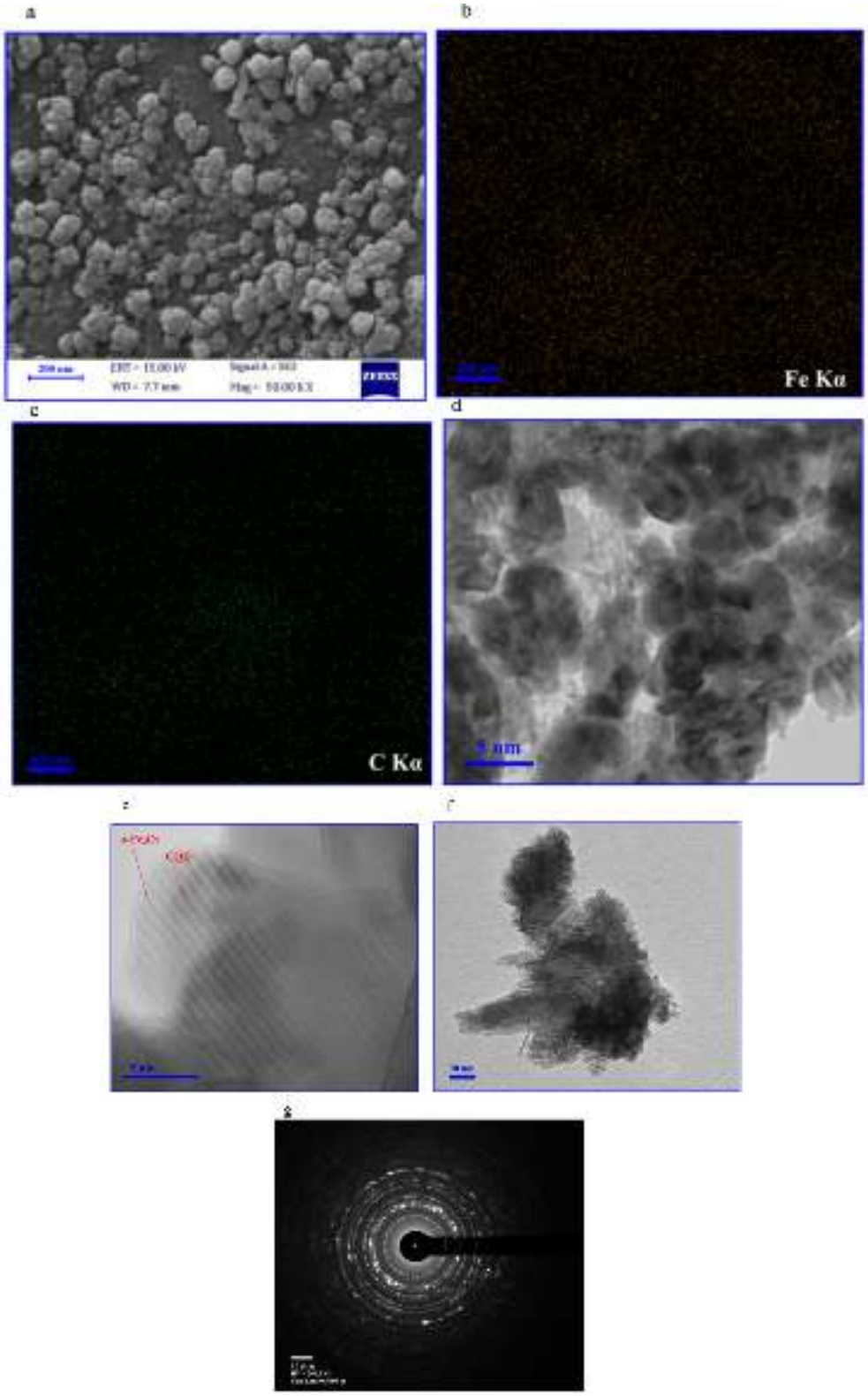

Fig. 4.

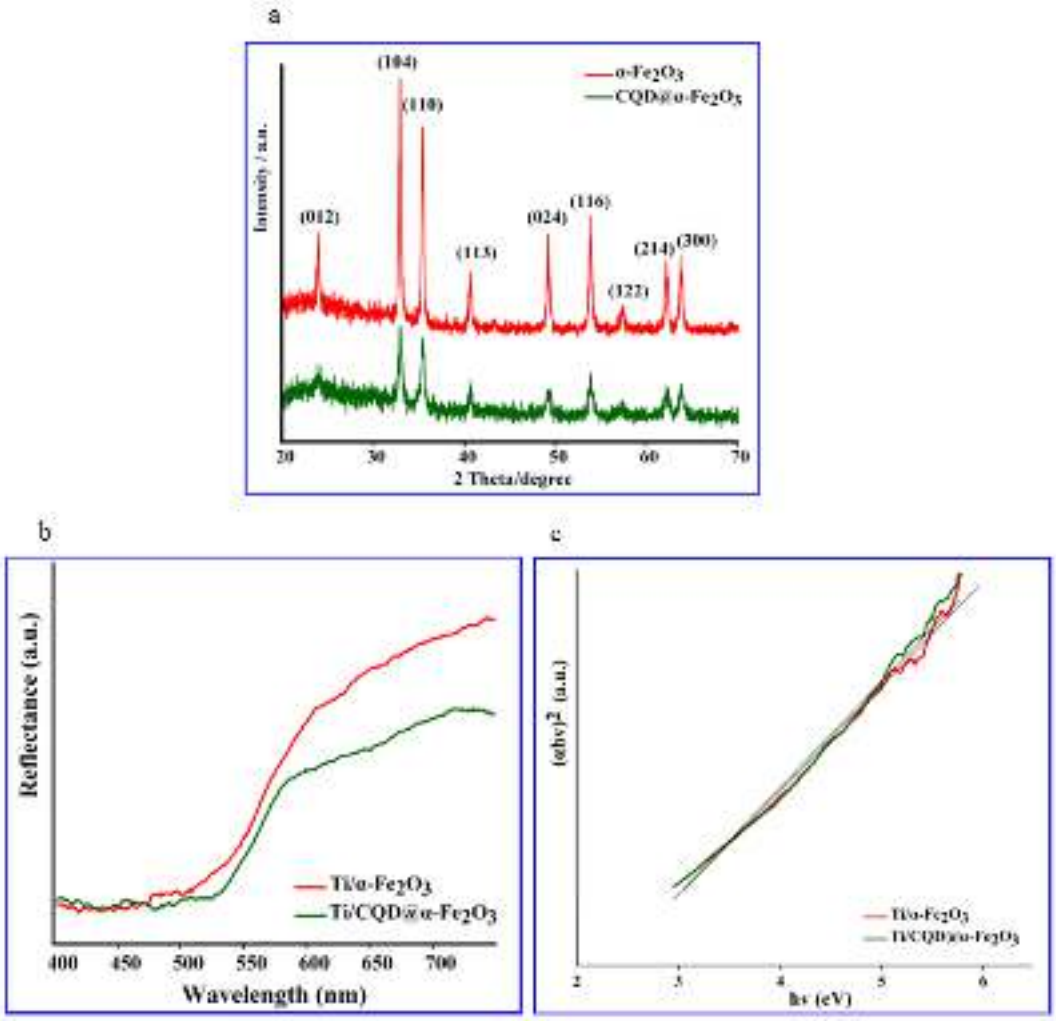
a
(104)
(110)
(012)
(113)
(024)
(116)
(122)
(214)
(300)
α-Fe2O3
CQDs@α-Fe2O3
Intensity / a.u.
20
30
40
50
60
70
2 Theta/degree
b
Reflectance (a.u.)
Ti/α-Fe2O3
Ti/CQD@α-Fe2O3
400
450
500
550
600
650
700
Wavelength (nm)
c
(αhν)2 (a.u.)
Ti/α-Fe2O3
Ti/CQD/α-Fe2O3
2
3
4
5
6
hν (eV)

Fig. 5.

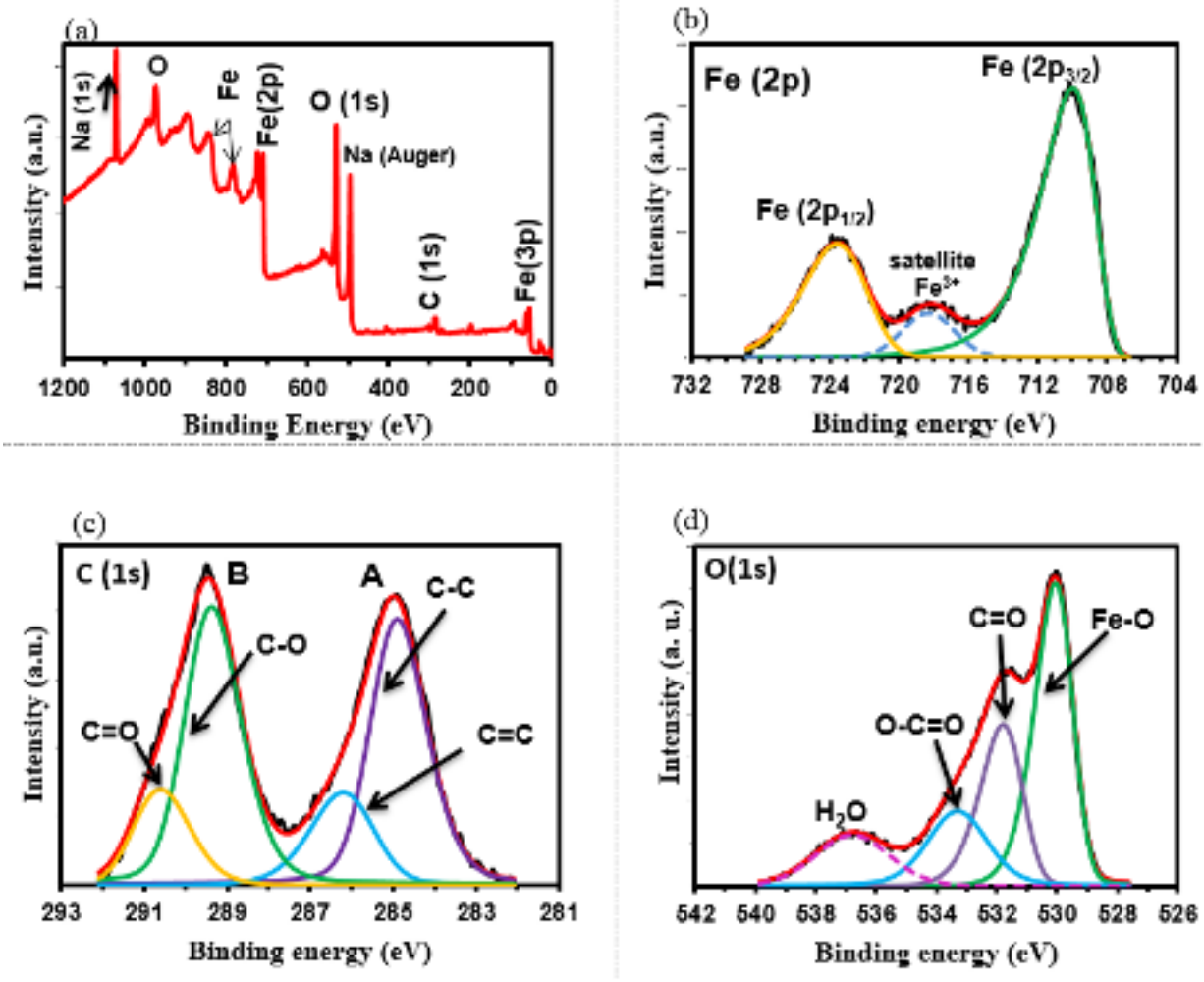
(a)
Na (1s)
O
Fe
Fe(2p)
O (1s)
Na (Auger)
C (1s)
Fe(3p)
Intensity (a.u.)
1200 1000 800 600 400 200 0
Binding Energy (eV)
(b)
Fe (2p)
Fe (2p3/2)
Fe (2p1/2)
satellite Fe3+
Intensity (a.u.)
732 728 724 720 716 712 708 704
Binding energy (eV)
(c)
C (1s)
B
A
C-C
C-O
C=O
C=C
Intensity (a.u.)
293 291 289 287 285 283 281
Binding energy (eV)
(d)
O(1s)
C=O
Fe-O
O-C=O
H2O
Intensity (a. u.)
542 540 538 536 534 532 530 528 526
Binding energy (eV)

Fig. 6

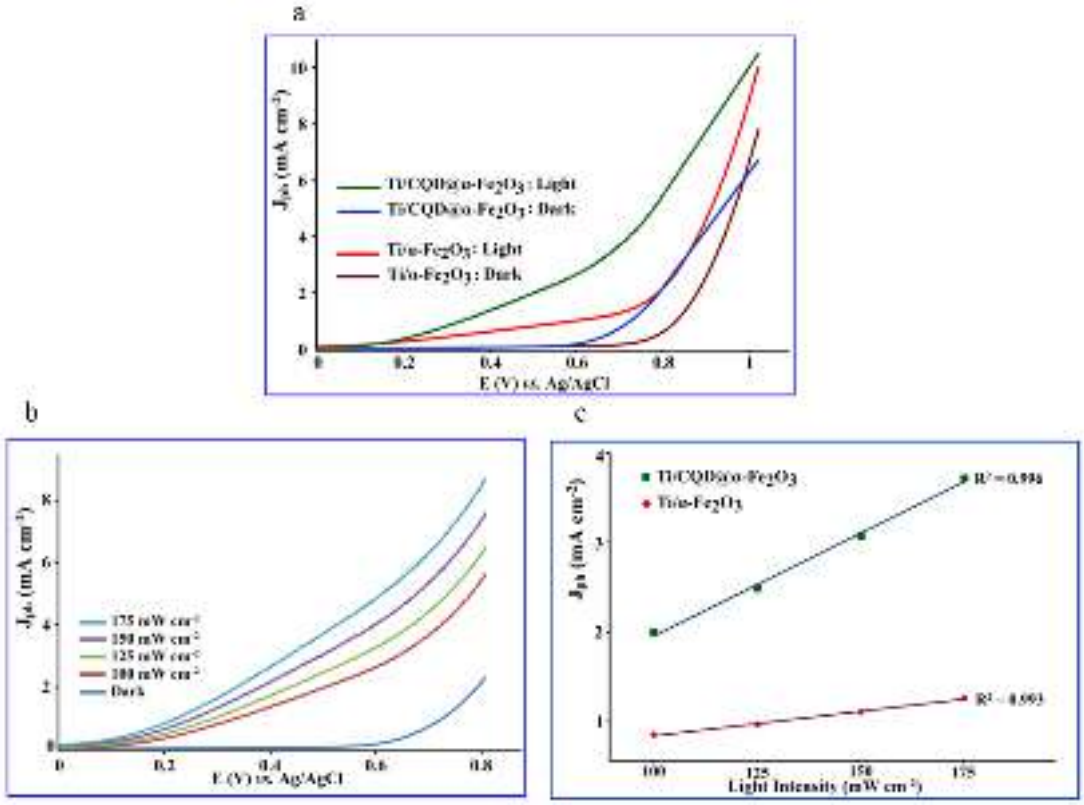

Fig. 7.

a

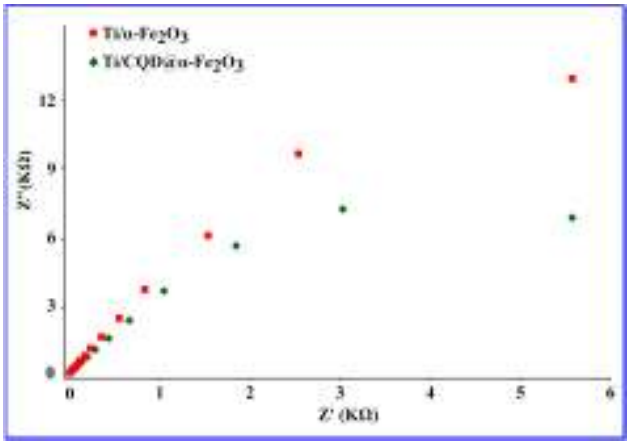

b

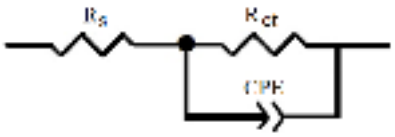

Sample	R_s (Ω)	R_{ct} (KΩ)	CPE (mF)
Ti/α-Fe_2O_3	31	90.9	1.52
Ti/CQDs/α-Fe_2O_3	14	5.7	1.57

Fig. 8.

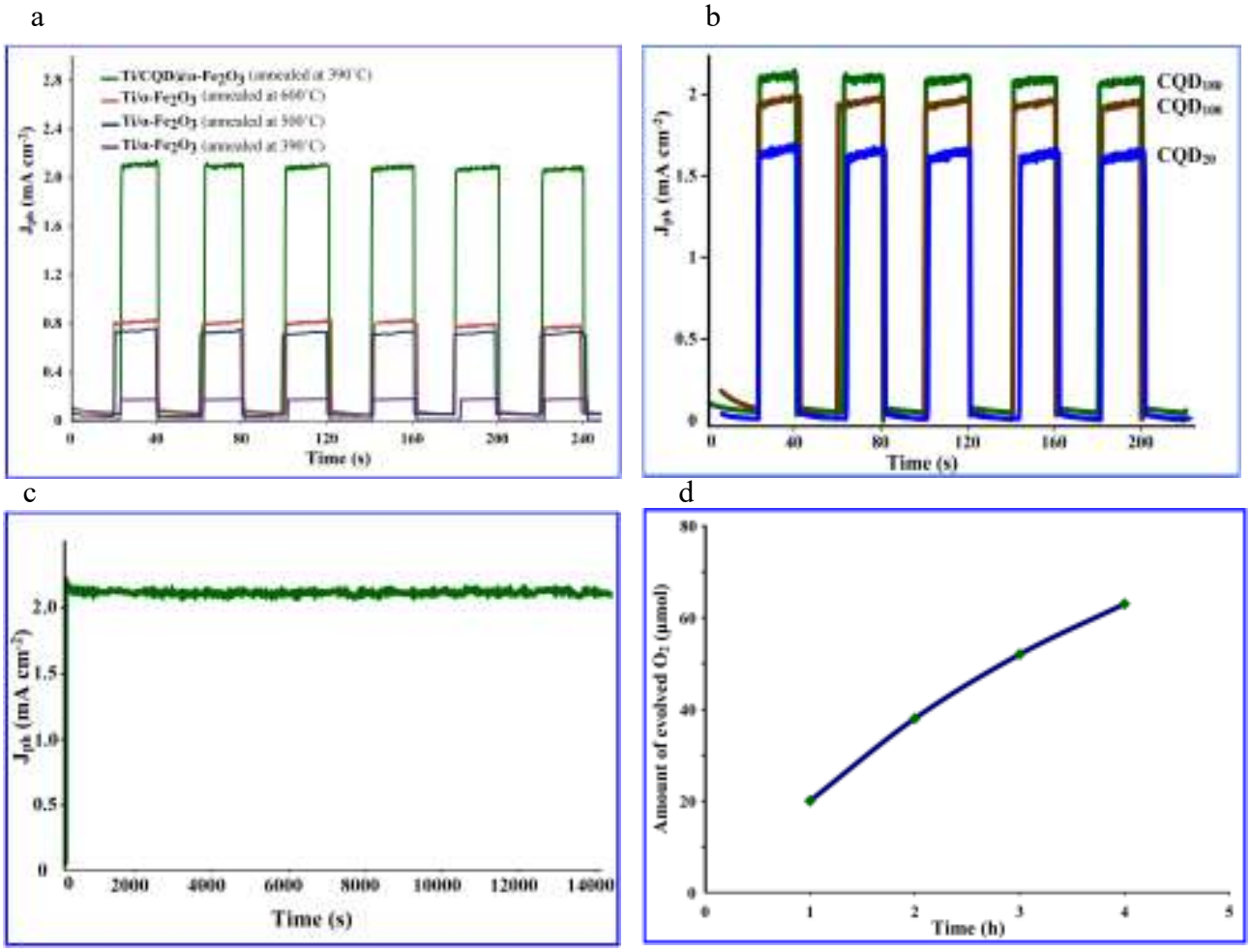
a
b
c
d
Time (s)
Time (h)
Amount of evolved O2 (μmol)
CQD100
CQD100
CQD20

Fig. 9.

a

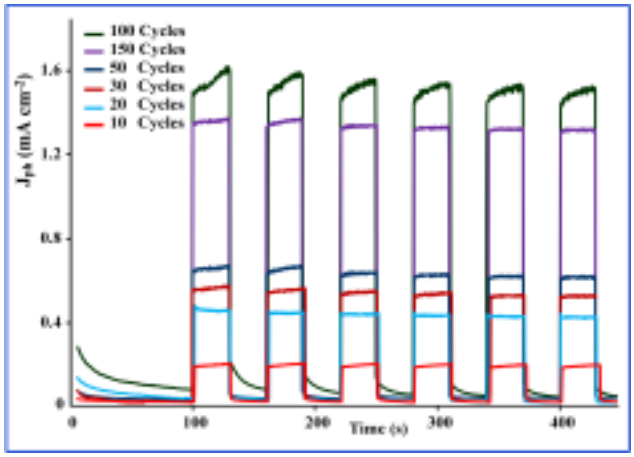
100 Cycles
150 Cycles
50 Cycles
30 Cycles
20 Cycles
10 Cycles
J_{ph} (mA cm^{-2})
Time (s)

b

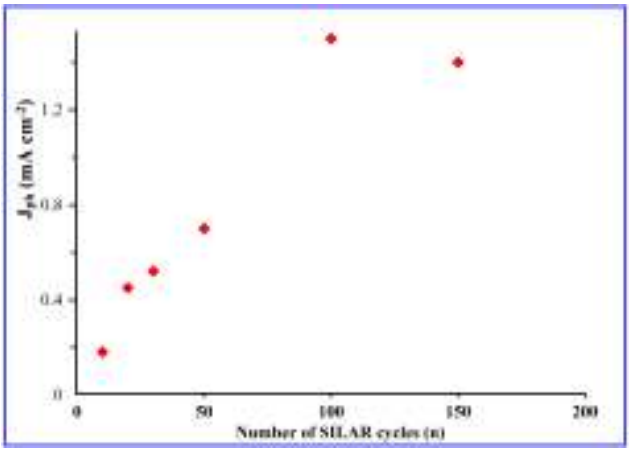
J_{ph} (mA cm^{-2})
Number of SILAR cycles (n)

Fig. 10.

a

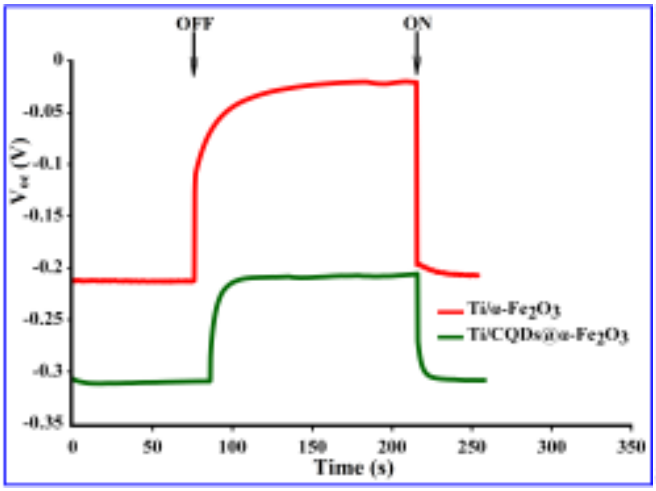
OFF
ON
0
-0.05
-0.1
-0.15
-0.2
-0.25
-0.3
-0.35
V_{oc} (V)
0
50
100
150
200
250
300
350
Time (s)
Ti/α-Fe2O3
Ti/CQDs@α-Fe2O3

b

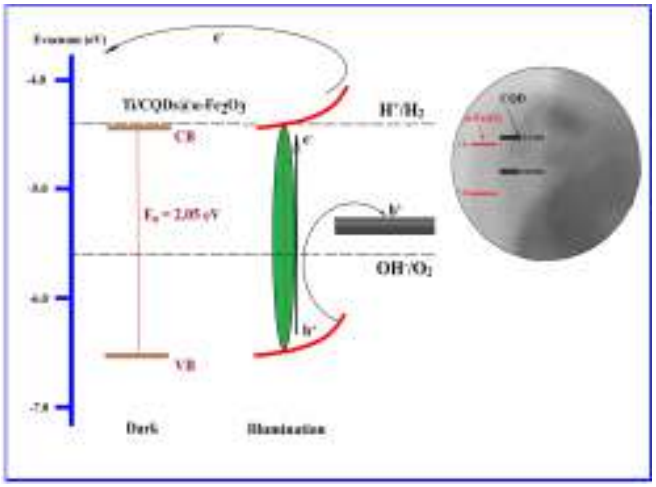
Ti/CQDs@α-Fe2O3
CB
VB
H+/H2
OH-/O2
Eg = 2.05 eV
e-
h+
Dark
Illumination
CQD

c

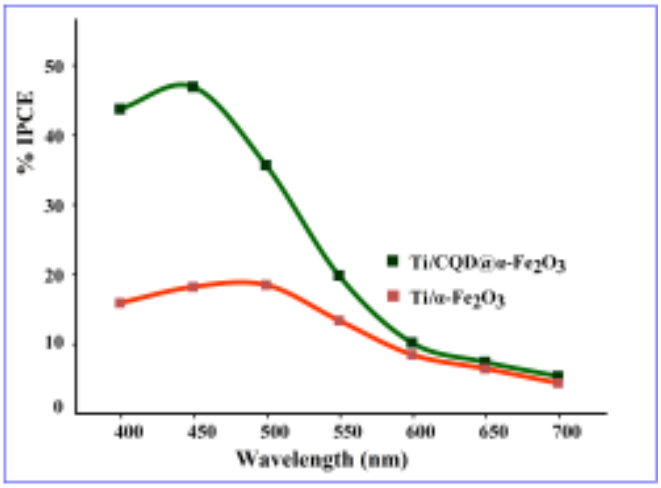
% IPCE
50
40
30
20
10
0
400
450
500
550
600
650
700
Wavelength (nm)
Ti/CQD@α-Fe2O3
Ti/α-Fe2O3

Tables

Table 1. The experimental conditions for the fabrication of six Ti/α-Fe_2O_3 samples by using hydrothermal method and their corresponding photocurrent densities (J_{ph}, $mAcm^{-2}$)

Sample	Fe^{3+} precursor concentration (M)	Hydrothermal reaction time (h)	Average film thickness (μm)	J_{ph} ($mAcm^{-2}$)
Ti/α-Fe_2O_3-L6h	5.0×10^{-2}	6.0	0.10	0.80
Ti/α-Fe_2O_3-H6h	1.5×10^{-1}	6.0	1.50	0.20
Ti/α-Fe_2O_3-L12h	5.0×10^{-2}	12.0	1.40	0.40
Ti/α-Fe_2O_3-H12h	1.5×10^{-1}	12.0	~ 5	0.10
Ti/α-Fe_2O_3-L24h	5.0×10^{-2}	24.0	~ 5	0.30
Ti/α-Fe_2O_3-H24h	1.5×10^{-1}	24.0	~ 6	0.20

Table 2. Comparison of the electrochemical and photoelectrochemical performances of Ti/CQD@α-Fe_2O_3 photoanode with previously reported α-Fe_2O_3-based photoanodes

Photoanode	Fabrication method	Modifier	Onset potential, E/V vs. RHE (E shift, mV)	Photocurrent density, mA cm^{-2} (E_{bias}, V)	Ref.
FTO/α-Fe_2O_3-Co-Pi	Electron beam evaporator	Cobalt-phosphate (Co-Pi)	0.810 (-185)	1.52 (+1.50)	36
FTO/Sn-doped α-Fe_2O_3	Hydrothermal	Doped Sn	0.80 (+150)	1.95 (+1.6)	37
FTO/α-Fe_2O_3-IrO_2 NPs	Chemical Vapor Deposition	IrO_2 nanoparticles (NPs)	0.80 (-200)	3.75 (+1.23)	38
FTO/α-Fe_2O_3-Co_3O_4 NPs	Hydrothermal	Co_3O_4 nanoparticles (NPs)	0.66 (-40)	1.20 (+1.23)	39
Fe/Sn-doped α-Fe_2O_3	Flame annealing	Doped Sn	0.70	1.1 (+1.23)	40
FTO/Ti-doped α-Fe_2O_3	Hydrolysis	Doped Ti	0.80 (-200)	1.83 (+1.02)	41
FTO/Ti-doped α-Fe_2O_3	SILAR	Doped Ti	0.92 (-80)	0.85 (+1.23)	42
FTO/QDs- α-Fe_2O_3	Hydrothermal	Hematite quantum dots	0.80 (-140)	1.60 (+1.6)	19
FTO/α-Fe_2O_3/CQD	Hydrothermal	Carbon quantum dots	0.9 (-300)	0.35 (+1.23)	43
FTO/CDots/Co3O4-Fe2O3	Hydrothermal	Carbon Nanodots (CDots)-Co_3O_4	0.79 (-60)	1.48 (+1.23)	34
ITO/C-coated α-Fe_2O_3	Electrodeposition	Coated Carbon	(-100)	2.1 (+0.4)	2
FTO/C-doped α-Fe_2O_3	Magnetron sputtering	Doped Carbon	-	1.18 (+0.6)	44
FTO/C-coated α-Fe_2O_3	Pyrolysis	Coated Carbon	0.7	2.1 (+1.23)	45
FTO/ α-Fe_2O_3/ RGO	Hydrolysis-solvothermal	Reduced Graphene oxide (RGO)	-	0.61 (+1.5)	46
Ti/@α-Fe_2O_3	SILAR	-	0.75 (-50)	1.5 (+0.70)	This work
Ti/CQD@α-Fe_2O_3	Hydrothermal	CQDs	0.65 (-150)	2.1 (+0.70)	This work

Table 3. Photocurrent densities (J_{ph}, $mAcm^{-2}$) of six Ti/α-Fe_2O_3 samples fabricated by using SILAR method at different number of cycles

Sample (Ti/α-Fe_2O_3-n)	**No. of SILAR Cycles (n)**	**J_{ph} ($mAcm^{-2}$)**
Ti/α-Fe_2O_3- 10	10	0.20
Ti/α-Fe_2O_3- 20	20	0.45
Ti/α-Fe_2O_3- 30	30	0.55
Ti/α-Fe_2O_3- 50	50	0.65
Ti/α-Fe_2O_3- 100	100	1.50
Ti/α-Fe_2O_3- 150	150	1.40